Grain interaction effects in polycrystalline Cu

C. Thorning[a,1], M.A.J. Somers[b] and J.A. Wert[a,*]

[a]Center for Fundamental Research: Metal Structures in Four Dimensions
Materials Research Department, Risø National Laboratory, 4000 Roskilde, Denmark

[b]Department of Manufacturing Engineering and Management
The Technical University of Denmark, Kemitorvet Building 204,
DK-2800 Kgs. Lyngby, Denmark

[1]now at Department of Materials Science and Engineering
Carnegie Mellon University, Pittsburgh, PA 15213, USA

Abstract

Crystal orientation maps for a grain in a deformed Cu polycrystal have been analysed with the goal of understanding the effect of grain interactions on orientation subdivision. The polycrystal was incrementally strained in tension to 5, 8, 15 and 25% extension; a crystal orientation map was measured after each strain increment. The measurements are represented as rotations from the initial crystal orientation. A coarse domain structure forms in the initial 5% strain increment and persists at higher strains. Crystal rotations for all coarse domains in the grain are consistent with the full range of Taylor solutions for axisymmetric strain; grain interactions are not required to account for the coarse domain structure. Special orientation domains extend 20 – 100 μm into the grain at various locations around its periphery. The special orientation domain morphologies include layers along boundary segments, lobes that may be further subdivided, and plates. Detailed analysis of the crystal rotations in the special domains provides strong evidence that they result from grain interactions.

*Corresponding author. Tel.: +45 4677 5824; fax: +45 4677 5758
 E-mail address: john.wert@risoe.dkT

1. Introduction

Classical plasticity theories propose that crystal rotation during plastic deformation of polycrystals depends on the macroscopic mechanical boundary conditions and on crystallographic factors in individual grains: the slip system geometry and initial crystal orientation. Neighbouring grains may influence the deformation process by creating, in essence, locally varying mechanical boundary conditions that differ from the macroscopic boundary conditions. The following paragraphs summarize effects ascribed to grain interactions in prior experimental and modelling studies of plastic flow in polycrystals.

If neighbouring grains substantially influence the plastic flow process, similarly oriented grains in different locations in a sample are expected to rotate differently and deviations from classical plasticity model predictions are expected. Such differences have been found in some investigations [1-5], although grain interaction is in some cases discounted as a likely explanation. Other studies found little effect of grain neighbourhood on crystal rotation [6,7]. A recent finite element analysis (FEA) model of grain aggregates suggests moderate grain interaction effects on plastic flow and crystal rotation in individual grains [8], but global texture evolution models that include effects attributed to grain interactions provide significantly better texture predictions than models that omit grain interactions [8-11]. At this time, it appears that neither models nor direct experimental observations conclusively identify the extent to which grain interactions affect crystal rotation in polycrystals.

A similar situation exists for grain subdivision. Maps of dislocation boundary structure [12-19], crystal orientation [20-26] and strain [27-31] within individual grains unequivocally demonstrate grain subdivision resulting from plastic flow. Some grain subdivision effects are

confined to the immediate vicinity of grain boundaries: slip traces [32-35], dislocation structure [12,13,17,36], crystal orientation [37-39], strain [27-31], and micro/nanohardness [31,40], have all been found to vary significantly within micrometers or 10's of micrometers of some grain boundaries. While attention is naturally drawn to cases where differences are observed, it is also worth noting that little evidence of grain interaction is found near many – perhaps most – grain boundaries. Nor are sharp strain gradients near grain boundaries the most prominent features in results from FEA models of grain-scale plastic flow [4,41-44]. Thus, although the localized gradients of dislocation structure, crystal orientation and strain near some grain boundaries are almost certainly grain interaction effects, these domains represent only a small fraction of the grain volume for materials with conventional grain sizes.

While localized effects are observed in the immediate vicinity of some grain boundaries, subdivision of whole grains into dislocation structure [12-18], crystal orientation [19-25], and strain component [26-30] domains is virtually a universal observation. The degree to which whole-grain subdivision is a consequence of grain interaction is uncertain. Whole-grain subdivision is a prominent feature of FEA model studies that examine individual grains in detail [41-44]. Results from a study by Beaudoin et al. [42] reveal subdivision of grains into domains with sharp boundaries (steep orientation gradients at domain boundaries). These studies were conducted by embedding one grain into a second grain of different crystal orientation. While useful for studying constraint effects, such geometries differ from the usual grain geometry in polycrystals where constraints change abruptly at triple grain junctions. The earlier model results of Harren and Asaro [41] reveal longer-range intragranular orientation gradients more frequently than abrupt gradients of the type found by Beaudoin et al. [42].

Other FEA modelling results incorporating many initial grain orientations suggest a modest role of grain interactions in the whole-grain subdivision process [8]. Further complicating interpretation of whole-grain subdivision observations is a proposed subdivision mechanism that does not invoke grain interactions. Plasticity models reveal that the total work of deformation can be reduced if grains subdivision into mutually cooperative domains that satisfy the mechanical boundary conditions as an ensemble, but not individually [45-47]. The alternating domain structures observed by TEM studies of dislocation boundaries, also found in the FEA results of Harren and Asaro [41], are taken as evidence of the cooperative accommodation mechanism. These disparate experimental and modelling results show that a consensus concerning the degree to which grain interaction effects influence the whole-grain subdivision process has, so far, not been achieved.

The present investigation has the goal of quantitative characterization of grain interaction effects through detailed examination of crystal orientation distributions in individual grains in polycrystalline Cu subjected to tensile deformation. The present article describes an assessment of one grain. The experimental results are compared to classical plasticity models that do not invoke grain interactions, and to prior models that sought to demonstrate grain interaction effects. An effort is made to deduce which of the various grain subdivision effects can be confidently attributed to grain interactions.

2. Experimental

A Cu tensile sample was prepared from an annealed Cu sheet of 99.99% purity. The 2.0 mm thick sheet was received from the manufacturer in the cold-rolled condition and was annealed

for 3.6 ks at 923 K to produce a recrystallised grain structure with a mean linear intercept

grain size of approximately 100 µm (all boundaries were included in the intercept counting

process). A flat tensile sample with gauge dimensions 25 mm long and 10 mm wide was cut

from the annealed sheet by electrodischarge machining; the tensile axis was parallel to the

original rolling direction. The shape of the tensile sample is illustrated in Fig. 1b together

with the coordinate designations: tensile axis = TA = specimen axis 1, front face normal = FF

= specimen axis 2, side face normal = SF = specimen axis 3.

The front surface of the tensile specimen was mechanically polished to a 3 µm diamond

finish. To remove residual mechanical deformation, a window on the front surface was

electropolished using an electrolyte of 250 ml H_3PO_4, 500 ml H_2O, 250 ml ethanol, 50 ml

propanol and 2 g CON_2H_4. Light reference scratches were made at the gauge section ends.

The polished specimen was examined in a JEOL® 5900 Scanning Electron Microscope

(SEM); an HKL® Electron BackScatter Diffraction (EBSD) system was used to measure grain

orientations on a square grid with a 2 µm step size. The grain orientation measurement

procedure was applied to several grains. The selected grains had maximum surface chord

lengths in the range of 200 – 400 µm, somewhat larger than the average grain size.

The experiment consisted of sequential deformation and analysis steps. The reference

scratches enabled accurate measurement of the mean axial plastic strain imposed on the gauge

section and helped to locate the selected grains when the sample was reintroduced into the

SEM after straining. Two practical problems became apparent as the experiment was

conducted. First, repeated scans of the same grains created carbon deposits that degraded

EBSD pattern quality. Chemical cleaning procedures were attempted with little success.

Second, surface roughness developed as a consequence of inhomogeneous plastic flow. This

led to inaccuracy of the identified crystal orientations because the sample – phosphorescent screen distance was not constant. In addition, the incident electron beam is translated in uniform steps relative to the sample surface. When a sample with a rough surface is tilted for EBSD measurements, the uniform electron beam displacements are transformed into an irregular grid of measurement points on the rough sample surface [48].

As a result of these complications, the experiment was conducted in two phases. The first phase includes results on the original specimen surface at 0, 0.05 and 0.08 accumulated axial plastic strain (denoted ε). In the second phase, the specimen was deformed to $\varepsilon = 0.15$ and the surface was re-prepared by light mechanical polishing with Struers OP-S$^{\circledR}$ colloidal silica polishing medium having a grain size of 0.04 μm. It was found by experimentation that mechanical disturbance of the surface layer after this polishing procedure was so slight that it did not significantly influence subsequent EBSD measurements. While the thickness of the rough surface layer removed by re-preparation is not known with certainly, it was substantially smaller than the mean grain size of 100 μm. Surface re-preparation was repeated after an additional strain increment to $\varepsilon = 0.25$. Since about half of the neighbouring grains had new orientations after the second re-preparation step, it is loosely estimated that 25 μm was removed from the surface during each re-preparation step. Since the geometries of the central grain and neighbouring grains change with depth, it is necessary to recall that the results for $\varepsilon = 0.15$ and $\varepsilon = 0.25$ represent different sections through the grain than results for lower ε.

3. Results

3.1. Rotation axis / angle maps for $\varepsilon = 0.05$ and 0.08

The grain, labelled α and shaded grey in Fig. 1a, is composed of two parts on the plane of polish, with an intervening annealing twin (β). The prominence of twin-related grain segments in annealed Cu has been previously described [49]. The mean orientation of the grain prior to straining was TA $= \left[0.694, 0.691, \overline{0.202} \right]$ and FF $= \left[\overline{0.524}, 0.293, \overline{0.800} \right]$, determined by quaternion averaging. For this grain the mean deviation of crystal orientation measurements from the average orientation was $0.54°$, a value characteristic of the accuracy of the EBSD method. This result includes measurements from both parts of the grain. Thus, prior to straining, the grain exhibited an orientation spread smaller than that detectable by the EBSD method. Table 1 lists the orientations of all neighbouring grains, β to σ, labelled in Fig. 1a. The table gives the orientations of the crystallographic directions parallel to TA and SF, the two specimen directions lying in the initial plane of polish, Fig. 1b.

After each plastic strain increment, crystal orientations were remeasured. The crystal orientation at each point was expressed as a rotation axis / angle pair, $\mathbf{R}/\Omega$, from the initial crystal orientation. The components of $\mathbf{R}$ are referred to the sample coordinate system. Taking the components of $\mathbf{R} = [r_{TA}, r_{FF}, r_{SF}]$ as red, green and blue (RGB) colour intensities, colour rotation axis maps (Figs. 1c, 1e, 1g) are generated for $\varepsilon = 0.05$, 0.08 and 0.15. Thus, locations where the crystal rotation is predominantly about TA are represented by high red intensity, predominantly FF rotations are represented by high green intensity, and predominantly SF rotations by high blue intensity. This method of associating colour with rotation axis components is illustrated by the pole figure in Fig. 1b. $\mathbf{R}$ is subject to significant uncertainty when Ω is less than $2°$, these points are shown as white. Regions outside of the

grain and invalid measurement points are shown as black. Corresponding greyscale maps

(Figs. 1d and 1f) represent the distribution of Ω, white corresponding to $\Omega = 0°$ and black to

12° crystal rotation.

A range of crystal orientations develops in each grain as plastic strain increases. Determining

the correct $\mathbf{R}/\Omega$ for a measurement point on the strained sample requires identifying the

original crystal orientation at that point; i.e. knowing which grain the material point was in

originally. An algorithm based on minimising the rotation angle during plastic deformation

has been used. This procedure works well for $\varepsilon = 0.05$ and 0.08 since the crystal rotation in

these cases is generally less than 10° from the initial crystal orientation. Thus, no

neighbouring grains appear in Fig. 1c – 1f. At $\varepsilon = 0.15$, however, the crystal rotation angles

were larger and the sample surface was re-prepared, exposing new neighbouring grains whose

orientation had not been measured prior to straining. These complications mean that it was

not possible to identify with certainty the grain of origin at $\varepsilon = 0.15$. Thus, some

neighbouring grains appear in Fig. 1g. The $\mathbf{R}/\Omega$ values for these neighbouring grains have no

physical significance since they refer to the initial crystal orientation of the central grain. The

results for $\varepsilon = 0.15$ and 0.25 are considered separately in Sections 3.5 and 3.6.

To attach physical significance to the $\mathbf{R}/\Omega$ variations in Fig. 1, crystal rotations at specific

points can be compared to the crystal rotations predicted by a crystal plasticity model. Fig. 2a

shows a series of locations marked 1 – 17 on the rotation axis map for $\varepsilon = 0.08$. Each point is

represented as a white circle enclosing a coloured dot. Points 1 – 10 are denoted by red

coloured dots; these are points within the body of the grain and are considered to represent the

range of crystal rotations characteristic of the grain as a whole. Points 11 – 12, 13 – 16 and

17 represent features A – C (marked on Fig. 1e) that appear to be associated with grain

boundaries or triple grain junctions. Features A – C are domains of larger than average crystal rotation, shown by their dark shade in Fig. 1f.

Fig. 2b is a stereographic projection representing the shift of tensile axis orientation for points 1 – 17 in the strain interval $\varepsilon = 0$ to $\varepsilon = 0.08$. The red lines in Fig. 2b correspond to points 1 – 10 which are identified by red dots in Fig. 2a, similarly for dots and lines of other colours. The grey polygon in the background of Fig. 2b corresponds to the full range of Taylor solutions [50,51] for an axisymmetric strain state with $\varepsilon = 0.08$ applied to the initial grain orientation. For a crystal with the initial orientation of grain α, four shear amplitude combinations with five nonzero shear amplitudes produce an axisymmetric strain state. These are listed as T1 – T4 in Table 2. Any linear combination of T1 – T4 also satisfies the imposed axisymmetric strain state. By imposing the Schmid tension constraint [52] for a specific shear amplitude combination, the crystal rotation corresponding to that shear amplitude combination is predicted. The grey polygon in Fig. 2b represents, for the selected initial crystal orientation, the range of final crystal orientations for all possible shear amplitude combinations giving rise to axisymmetric strain. In the present article, such loci of final crystal orientations are referred to as the *full range of Taylor solutions* for a given imposed strain state.

Analysis of points 1 – 17 leads to the following conclusions:

i. The tensile axis rotation directions for points 1 – 10 are within the full range of Taylor solutions, although the rotation angles appear to be somewhat larger than predicted by the Taylor model [2]. Since points 1 – 10 are broadly representative of the various orientation domains into which the crystal subdivides during tensile deformation, it is concluded that

    the tensile axis rotations characteristic of the broad orientation domains in this grain

    conform to the full range of Taylor solutions.

ii. The shifts of tensile axis orientation for the points associated with features A – C are all

    outside the full range of Taylor solutions, with the exception of point 11.

Several supplemental observations can be made. First, note that conclusion i would be substantially altered if a single Taylor solution were considered. Various methods have been devised to eliminate the multiplicity of Taylor solutions for specific initial grain orientations; these include the average Taylor solution [53], Taylor solutions including latent hardening effects [54], models derived from the generalized Taylor model of Asaro and Needleman [55] and a second order work hypothesis [56,57]. However, when comparing experimental crystal rotations to the model results, it appears to be appropriate to use the full range of Taylor solutions to assess whether or not observed crystal rotations are consistent with the classical Taylor model.

Second, it was noted earlier that features A – C have a dark shade in Fig. 1f, indicating larger than average crystal rotations. However, the tensile axis rotation indicated in Fig. 2b is not greater than average for specific points in regions A – C. This difference arises because the shift of tensile axis orientation illustrated in Fig. 2b accounts for only part of the total crystal rotation.

Since features A – C appear to emanate from grain boundaries, it is possible that the uncharacteristic crystal rotations identified in these regions result from grain interactions. To examine this possibility, more detailed analysis of these regions has been performed, including analysis of neighbouring grains.

3.2. Analysis of crystal rotations in the neighbourhood of feature A

Fig. 3a shows a rotation axis map for the region around feature A at $\varepsilon = 0.08$. In Figs. 1 and 2, neighbouring grains were excluded to the greatest extent possible to draw attention to the features in grain α. In Fig. 3, rotation axes in neighbouring grains are included to allow correlated observations across grain boundaries. Grain boundaries are not necessarily apparent in rotation axis maps spanning multiple grains; white lines showing grain boundary locations are superposed on the maps in Fig. 3. The yellow lines are reference lines showing the points included in the plots to the right and left of the rotation axis map.

The right yellow reference line and associated plots show the variation of **R** components and Ω in the vicinity of feature A. The dominant rotation component is r_{FF} (green), which is negative in the lower domain of feature A (point 11) and positive in the upper domain (point 12). This indicates that opposing crystal rotations occurred in the lower and upper domains, amplifying the conclusion from Fig. 2b that shows reversed rotation the tensile axis. The transition between the two domains is abrupt, within one measurement step (2 μm) at the location of the yellow line.

The left yellow reference line passes through adjacent grain δ. The analysis shows that grain δ is subdivided into lower and upper domains. The dominant rotation component in the lower domain is $r_{FF} < 0$ (green) and in the upper domain is $r_{SF} < 0$ (blue). This transition is also abrupt; i.e., less than the measurement spacing distance. The crystal rotation discontinuities in grains α and δ meet at the same location on the grain boundary.

3.3. Analysis of crystal rotations in the neighbourhood of feature B

Fig. 3b shows a similar analysis for feature B. In Fig. 1e feature B is a 100 μm long plate extending from near a triple grain junction along the lower edge of the grain nearly to the grain corner at the upper right. The rotation axis map in Fig. 4b shows the lower portion of feature B. The right yellow reference line passes through feature B and shows that it is a domain of rotation axes with mixed r_{FF} and r_{TA} components, whereas the domains in grain α both above and below feature B exhibit mixed r_{SF} and r_{TA} components. This difference in **R** corresponds to the difference in shift of the tensile axis rotation between point 17 and points 9 and 10 in Fig. 2b.

Neighbouring grain σ has a tensile axis close to [100] and thus exhibits small rotation angles. (Rotation angles are only a few degrees throughout this grain. The requirement of a 2° rotation angle for a point to be considered as a valid measurement point was relaxed in preparing the rotation axis map in Fig. 2b. The short-range variations of **R** close to the boundary are almost certainly noise associated with small Ω.) While the uncertainty in **R** is large in grain σ, the rotation axis map and associated graphs show rotations dominated by r_{SF} < 0 far from the grain boundary (location S) and a mixture of rotations in the neighbourhood of the triple grain junction. For example, location T exhibits prominent r_{SF} > 0 component, opposite to the characteristic r_{SF} < 0 component that dominates far from the triple grain junction (S). Locations U and V exhibit prominent r_{FF} components of opposite sign, both departing from the characteristic r_{SF} < 0 component that dominates far from the triple grain junction (S). In contrast to the variations in crystal rotation observed in grains α and σ, little change occurs in the twin (β) upon approaching the triple grain junction. The wide range of crystal rotations detected in grain σ is likely to reflect the large dependence of crystal rotation

on local mechanical boundary conditions previously found for grains having low Taylor factors [5,8,58].

3.4. Analysis of crystal rotations in the neighbourhood of feature C

Feature C is characterised by a pair of interlocking rotation axis domains; points 13, 14 and points 15, 16 in Fig. 1; both of which exhibit tensile axis rotations opposite to the general trend throughout grain α. The characteristics of this region differ somewhat from those found for feature A. The two prominent r_{TA} rotation regions (red) of feature C, through which the left reference line passes, have the same sense of crystal rotation about TA, and the two prominent r_{FF} rotation regions (green) through which the right reference line passes have the same sense of crystal rotation about FF. Thus, the upper and lower red regions constitute a single domain and the upper and lower green regions constitute a second domain.

The upper end of feature B appears near the bottom of Fig. 3c. At the position where the left reference line passes just ahead of feature B, a slight increase in $r_{FF} > 0$ is recorded. This is consistent with the observations from Section 3.3 showing that $r_{FF} > 0$ is the dominant **R** component for feature B.

3.5. Rotation axis map for $\varepsilon = 0.15$

Fig. 1g shows a rotation axis map for $\varepsilon = 0.15$. Several neighbouring grains appear in this rotation axis map; recall that no physical meaning should be attached to **R** for those grains. Dashed white lines are used to delineate the grain boundary at locations where neighbouring grains abut.

Features A – C are readily identifiable on a plane of polish that was originally about 25 μm below the surface. The geometry of the features has changed moderately. In particular, feature B appears to be more strongly associated with the grain boundary at the upper right than with the triple grain junction along the lower edge of the grain.

Two new features are labelled D and E. feature D appears in the vicinity of a triple grain junction. Feature E represents a layer-like crystal orientation domain parallel to a grain boundary segment; the extent of feature E correlates strongly with an adjacent twin.

While several new features appeared after the additional strain increment and surface re-preparation, many features from the original observations at lower ε are readily identifiable. The coarse orientation domains can be identified. The boundaries of coarse domains are diffuse; i.e., the orientation transitions are accommodated over distances of 10's of micrometers. On the other hand, features A – C have somewhat sharper boundaries than observed on the original surface at $\varepsilon = 0.08$. This is also a characteristic of feature E, which appears as an orientation domain that has virtually seceded from grain α. The boundary between feature E and the original grain represents a misorientation of 18° and is 2 – 6 μm (1 to 3 grid points) wide.

3.6 Rotation axis / angle maps for $\varepsilon = 0.25$

Figs. 4a and b show rotation axis / angle maps of the grain for $\varepsilon = 0.25$. As described earlier, the specimen surface was re-prepared again after the strain increment from $\varepsilon = 0.15$ to $\varepsilon = 0.25$; the thickness of the layer removed in this step is also estimated to be 25 μm. The

combination of increased strain and removal of a 50 μm surface layer (total for two re-preparation steps) have resulted in substantial changes in the geometry of the twin and the neighbouring grains. The rotation axis map for $\varepsilon = 0.25$ reveals subdivision of the grain into three or four coarse domains, as well as the appearance of special **R** domains in the vicinity of some grain boundaries. While the geometry of the coarse domains and special domains near grain boundaries differs from that seen at lower ε and a different section plane, there are no substantive differences in these aspects of the crystal orientation structure.

In addition to the coarse domains and special domains near grain boundaries, a fine lamellar structure appears within the coarse domains. These lamellae are particularly evident in the rotation angle map, but they also appear in some regions in the rotation axis map. These lamellae represent subdivision of the original grain at a different length scale than the coarse domains. They have a width on the order of several measurement spacings, roughly 5 μm. The four slip traces for the initial grain orientation are shown at the lower right in Fig. 4b: it is seen that one set of lamellae are approximately parallel to slip trace from the a slip plane, (111), but the other set of lamellae are not parallel to any of the slip plane traces. Fig. 4c uses a different colour scheme for crystal orientation representation; this is described in Section 4.4.

4. Discussion

4.1. Coarse domains

By identifying in Fig. 1 regions of similar tensile axis rotation, Fig. 5 was drawn to schematically represent subdivision of the grain into 5 coarse crystal orientation domains. Points 1, 2, 5 lie in a domain of mainly r_{SF} crystal rotation, points 3 and 4 lie in a domain of

r_{TA} + r_{FF} crystal rotation, and point 6 lies in a domain of r_{TA} + r_{SF} crystal rotation. In the other part of the grain, two crystal orientation domains are identified, one containing points 7, 8, 9 to left and above feature B and one containing point 10 to the right and below feature B. Some variation of **R** occurs within each of the identified coarse domains and alternate coarse subdivision schemes for the grain are possible; a rigorous method for identifying the coarse domain structure in rotation axis / angle maps has not been developed. However, the following comparison does not depend on the exact number of coarse domains identified.

Table 2 contains results relevant to consideration of the origin of coarse domains. In the left column of the table are shown 3 strain states: an axisymmetric strain state and two strain states combining a shear strain component with axisymmetric normal strain components. The next column contains a numerical factor, M, corresponding to the Taylor factor in the axisymmetric strain case. The remaining columns contain shear amplitude fractions, f^k for slip system k, from which the shear amplitude, γ^k, for an imposed axial strain (ε) can be found from the relation:

$$\gamma^k = M\varepsilon\left(\frac{f^k}{100}\right) \tag{1}$$

Fig. 2 showed that the tensile axis rotation directions for points 1 – 10 are consistent with the full range of Taylor solutions for axisymmetric strain, although the rotation angles are slightly larger than predicted by the Taylor model. Since points 1 – 10 were selected as representative examples of the various coarse domains, we surmise that the tensile axis rotations throughout all of the coarse domains are consistent with the full range of Taylor solutions for axisymmetric strain. No variation of strain state is associated with Taylor solutions T1 – T4.

Thus, no variation in strain state, arising from grain interaction effects, or any other source, is required to account for the coarse domains.

Additional observations suggest a modest role of grain interactions in development of coarse domains. Firstly, the diffuse coarse domain boundaries do not always intersect the periphery of the grain at a triple grain junction. An example of this is the coarse domain boundary between points 5 and 6 near the lower edge of the grain. Secondly, there is no evidence in Fig. 1 that the crystal rotations associated with a coarse domain are more intense near grain boundaries than in the core of the grain.

The conclusion that the coarse domain structure is modestly influenced by grain interactions is in concert with the conclusion from recent modelling work by Poulsen et al. [3] and Raabe et al. [8] who suggested a minor effect of grain interactions on grain subdivision. It also appears to be consistent with FEA model results showing intense localized grain interaction zones, but rather diffuse orientation gradients extending throughout the grains (for example Figs. 10 – 12 in Ref. [41]). On the other hand, grain interaction was interpreted as having a strong effect on formation of coarse orientation domains in a bicrystal model in which one grain was embedded in a second grain [42]. The latter study, however, departs from the grain geometry considered in the present case: the model is constructed such that the same grain adjoins all faces of the central grain; there are no triple grain junctions.

We deduce from evaluation of the present experimental observations that grain interaction has at most a moderate effect on subdivision of the grain into a coarse domain structure. This conclusion is, at present, restricted to the grain neighbourhood analysed in detail in the this article; factors such as grain size and texture could change the degree to which grain

interaction influences the coarse domain structure. Since qualitatively similar coarse domain structures are observed on the original free surface and after each surface re-preparation step, we believe that the coarse domain structures observed at all strain levels are not phenomena associated strictly with the free surface.

4.2. Grain interaction domains.

Features A – E in Fig. 1 represent special crystal rotation domains, identified as such because crystal rotations in these regions deviate strongly from those observed in the rest of the grain.

Feature A. The abrupt boundary formed between the two rotation domains of feature A resembles the subgrain boundary found in the results obtained with an FEA model by Harren and Asaro [41]. In part of their investigation, a 2D initially hexagonal grain array was subjected to simple shear. The following interpretation was not given in Ref. [41], but is made here to facilitate comparison with the present experimental results. The trace of the most active slip system is substantially different in two neighbouring grains (14 and 19 in Fig. 11, Ref. [41]). The two grains thus respond differently to the applied strain, with the result that a shear stress may develop parallel to the grain boundary. Curvature of the slip plane traces in one of the grains (14 in Ref. [41]) provides evidence for the constraining effect of the neighbouring grain (19 in Ref. [41]). Consequently, a sharp rotation gradient – a subgrain boundary – projects into a third grain (15 in Ref. [41]) as an extension of the grain boundary. In feature A in the present investigation, different shear amplitude sets in the upper and lower parts of neighbouring grain δ are reflected by subdivision of grain δ, and a sharp boundary is induced between two zones of opposite rotation as a projection of the subdivided

neighbouring grain. No explanation other than grain interaction readily accounts for the correspondence of orientation domains in adjoining grains α and δ.

Feature B. In the original surface section, $\varepsilon = 0.08$ (Fig. 1e,f), this lenticular feature lies between a triple grain junction on the lower edge of the grain and the grain corner at the upper right. The crystal rotation pattern within the twin (β)does not appear to be significantly perturbed, but a complex crystal rotation pattern is present in neighbouring grain σ. In the section about 25 μm below the original surface, $\varepsilon = 0.15$ (Fig. 1g), this lenticular feature appears more strongly associated with the triple grain junction at the upper right of grain α, and the point of intersection with the lower edge of grain α has shifted away from the twin. In the section about 50 μm below the original surface, $\varepsilon = 0.25$ (Fig. 4), this feature is not observed. We surmise that feature B was inclined in such a way that it exited the right edge of the grain at a depth between ca. 25 and 50 μm below the original surface.

Feature C. The two interlocking domains both exhibit **R** inconsistent with an axisymmetric strain state. Four boundaries between adjoining grains meet in this corner of the grain. At point Z in Fig. 3c, the boundary between adjacent grains μ and ν aligns with the boundary between r_{TA} and r_{FF} domains in feature C. The mechanism responsible for formation of feature C could be similar to that found in prior model results [41].

Feature D. This feature corresponds to an extension of the boundary between two adjoining grains. Slight differences in the strain states in the adjoining grains could be expected to produce a lobe-shaped region of differing strain state extending into the grain as an extension of the grain boundary. The mechanism responsible for formation of feature D may also be similar to that illustrated in the prior model results [41].

Feature E. A distinct layer of 20 μm thickness has formed in precise correspondence with a twin in adjoining grain η. A layer of 20 μm thickness resembles the localized grain boundary interaction zones detected by TEM [36] and by recent experiments in which localized strain states were found in grain boundary layers [27-29].

Table 2 shows the four shear amplitude combinations with five nonzero shear amplitudes that produce the required axisymmetric strain state: T1 – T4. It has previously been shown in Fig. 2 that the crystal rotations in features A – C (points 12 – 17) are inconsistent with the full range of Taylor solutions for an axisymmetric strain state. Various simple modifications of the axisymmetric strain state were tested by trial and error; these included deviations from axisymmetry and various magnitudes of each shear strain component. Among the modifications tested were the strain states listed in the lower two sections of Table 2, T5 – T8 and T9 – T12. Fig. 6a is a stereographic projection showing the observed tensile axis rotations for points 12, 15, 16, 17 superposed on the polygon specifying tensile axis rotations for the full range of Taylor solutions corresponding to a strain state with $\varepsilon_{12} > 0$ listed in Table 2. Similarly, Fig. 6b shows the observed tensile axis rotations for points 13 and 14 superposed on tensile axis rotations corresponding to the full range of Taylor solutions for the strain state with $\varepsilon_{13} < 0$. Fig. 6c shows the observed tensile axis rotations for features D and E and tensile axis rotations corresponding to the full range of Taylor solutions for the strain state with $\varepsilon_{13} < 0$.

The correspondence of experimental and model strain states shown in Fig. 6 does not prove that these specific nonaxisymmetric strain states were present in features A – E. However, these features are special **R** domains that emanate from grain boundaries and they exhibit

crystal rotations departing significantly from those found in other parts of the grain. Features A – E appear where a neighbouring grain is subdivided, in the vicinity of one or more triple grain junctions, or occupy the length of the grain boundary where a single neighbouring grain abuts the central grain. We thus attribute the special **R** domains that comprise features A – E to grain interactions. Since qualitatively similar grain interaction domains are observed on the original free surface and after each surface re-preparation step, we believe that the grain interaction domains observed at all strain levels are not phenomena associated strictly with the free surface.

The present observations can be compared with prior experimental observations and model results illustrating grain interaction effects. For reasons delineated in Section 4.4, previous crystal orientation mapping methods have not revealed 50 – 100 μm lobe and plate-shaped grain interaction domains. TEM observations have mainly revealed narrow interaction layers similar to feature E [36]. Recently developed strain mapping methods occasionally reveal features that resemble the lobe-shaped grain interaction domains reported in the present article; for example Fig. 7 of Ref. [28]. However, von Mises strain maps, as are often presented, may mask the prevalence of lobe- or plate-shaped interaction zones as a result of the averaging effect associated with calculation of the von Mises strain from the individual strain tensor components.

4.3. Relationship to prior studies of dislocation structure

When polycrystalline samples are deformed to intermediate strains, by rolling for example, a lamellar boundary structure forms, consisting of high-angle boundaries mostly parallel to the rolling plane [19,59]. The original grain boundaries constitute 20 or 30% of the lamellar

boundaries; the remainder of the high-angle boundaries are thought to be introduced by grain subdivision [59]. The three to five coarse domains identified in the grain for ε in the range 0.05 to 0.25 correspond well with the high angle boundary fraction reported in rolled samples after intermediate strains [59]. Since both sets of observations are made on 2D sections containing the extension axis, the larger number of coarse domains that may be present in the volume of the grain does not influence the comparison. The correspondence noted here suggests that the coarse domain structure represents the initial stage of grain subdivision that ultimately produces the layered texture-component structure commonly associated with intermediate rolling strains.

The fine lamellar structure, one set of lamellae being parallel to the trace of slip plane a, also resembles structures reported in deformed metals. Most grains in Al, Cu and Ni deformed in tension to ε greater than about 0.10 exhibit a rather uniform structure consisting of long dislocation boundaries, referred to as geometrically necessary boundaries (GNBs) [19]. Either one set or two intersecting sets of GNBs form, depending on the initial grain orientation [15,17]. Equiaxed dislocation cells form between GNBs. For grains oriented with the tensile axis near [100], extended dislocation boundaries do not form; the dislocation structure consists of equiaxed dislocation cells [15,17]. However this observation is not relevant for grain α having TA $= \left[0.694, 0.691, \overline{0.202} \right]$.

GNBs have been found to form approximately parallel to the slip plane corresponding to the largest Schmid factor [17]. This often, although not always, corresponds to the slip plane exhibiting the largest total shear amplitude. Table 2 shows the correspondence between the four shear amplitude combinations with five nonzero shear amplitudes that produce the required axisymmetric strain state, T1 – T4, and the Schmid factors, m, from a uniaxial stress

analysis applied to the initial crystal orientation. The largest total shear amplitudes are found for slip systems with a slip plane, and the slip systems with this slip plane also have the largest Schmid factors. One set of lamellae in Fig. 4b is also roughly parallel to the a slip trace.

The spacing of GNBs varies with strain, but is reported to be near 1 μm for high-purity Cu deformed in tension to $\varepsilon = 0.22$ [17]. That compares to the lamellar thickness of roughly 5 μm estimated from Fig. 4. TEM observations show that a significant fraction of the GNBs in Cu strained to $\varepsilon = 0.22$ represent misorientations of 1° or less [19]. Such small misorientations are below the angular resolution limit of the EBSD method [20] and thus would not be expected to appear in Fig. 4. Based on the correspondence between slip trace and lamellae orientations, and a reasonable explanation of a lamellar spacing larger than the GNB spacing observed by TEM, we interpret the fine lamellar structure parallel to slip trace a to represent a fraction of the GNBs detected by TEM.

The second set of lamellar features is not parallel to slip traces. These lamellae may also represent portions of an intersecting set of GNBs that do not form parallel to a slip plane. Several interpretations of such "macroscopically oriented" GNBs have been suggested [60,61], but it is not possible at this point to reliably interpret the orientation of the second set of lamellae.

Prior TEM observations show that the GNB structure depends on grain orientation [15,17], but the GNB structure does not generally reflect grain subdivision at the scale of coarse domains and grain interaction domains [17]. The uniform nature of the GNB structure within individual grains could be interpreted as indicating that coarse domains do not form and grain

interaction domains are confined to local effects in the immediate vicinity of grain boundaries. However, Table 2 provides a way to reconcile the crystal orientation and GNB observations. In spite of the significant difference in **R** among the coarse domains, solutions T1 – T4 all have the highest total shear amplitude on the *a* slip plane. Thus, although significant rotation differences develop within a set of coarse domains deforming by combinations of shear amplitude sets T1 – T4, a uniform GNB structure with GNBs parallel to plane *a* could form throughout all of the coarse domains. In addition, slip plane *a* has the largest total shear amplitude for 2 of the 4 solutions T5 – T8, and 2 of the 4 solutions T9 – T12, which are consistent with tensile axis rotations observed in the grain interaction domains. This analysis shows that it is possible, although not required, that the entire grain would exhibit GNBs parallel to slip plane *a*, despite the presence of a rich domain structure detectable in rotation axis / angle maps. This analysis suggests that GNB structure is not a sensitive indicator of shear amplitude differences that give rise to a wide variety of crystal rotations.

4.4. Analysis technique

Numerous prior studies have used crystal orientation maps to investigate intragranular structure evolution during deformation. However, features A – E, which are interpreted here as grain interaction features, are generally absent in crystal orientation maps published previously. Fig. 4 illustrates one reason why features of these types may have been previously overlooked. As described in Section 3.6, Figs. 4a and 4b are rotation axis and rotation angle maps for $\varepsilon = 0.25$. The colour coding method used in Fig. 4a is that described in Section 3.1 and illustrated in Fig. 1b: the rotation axis components expressed relative to the specimen coordinate system (TA, FF, SF) are mapped into the RGB colour space.

In an effort to avoid effects associated with the sample surface, polycrystalline samples are generally sectioned after deformation. As a consequence, the original grain orientation is not known and rotation axis / angle maps cannot be plotted. Instead, it has been common to plot the absolute crystal orientation (for example Ref. [21]), rather than the change of crystal orientation associated with deformation. Fig. 4c shows the result of a common technique: mapping the crystal direction parallel to a sample axis onto an RGB colour space. Fig. 4c was prepared by mapping the crystal direction corresponding to TA into the standard stereographic triangle and subsequently colour coding by assigning [100] = red, [110] = green and [111] = blue, as illustrated by the stereographic triangle inset in Fig. 4c. The result of such a mapping process is that the coarse domains and nearly all of the grain interaction features are unresolved. Comparing Figs. 4a and 4c shows unequivocally the advantage of the rotation axis / angle mapping technique for revealing many aspects of the crystal orientation subdivision process.

5. Conclusions

Crystal orientation maps for a grain in a Cu polycrystal have been analysed in detail with the goal of identifying the grain interaction effects in the orientation subdivision process. The following conclusions apply to results for this grain.

(i)   A coarse domain structure forms during the initial 5% plastic strain increment and persists at higher strains. The domains have diffuse boundaries that cannot be associated with crystallographic planes. Crystal rotations within all coarse domains in the grain are consistent with the full range of Taylor solutions for axisymmetric strain. Grain interactions are not required to account for the coarse domain structure.

(ii)   The coarse domain structure persists without significant refinement over the ε range 0.05 to 0.25. A fine lamellar structure internally subdivides the coarse domains at higher strains. The orientation of lamellae indicates that they correspond to part of the GNB structure commonly observed by TEM.

(iii)   Features of size scale 20 – 100 μm form at various locations around the periphery of the grain. The feature morphologies include layers along a boundary segment, lobes that may be further subdivided, and plates. The crystal rotations within all of the identified features are inconsistent with the full range of Taylor solutions for axisymmetric strain. Detailed analysis of the crystal orientation maps for the grain neighbourhood show that the features can be directly associated with intersecting grain boundaries, intersecting grains, or domain structures in adjacent grains. These features are considered to be grain interaction domains.

(iv)   Based on current understanding of the connection between shear amplitudes and the morphology of geometrically necessary boundaries, differences in GNB structure among the coarse domains, and among the grain interaction features are not required. GNB structure is not a sensitive indicator of grain interaction effects for this grain.

References

1. C.S. Barrett, L.H. Levenson, Trans AIME, **137** (1940) 112.

2. S. Panchanadeeswaran, R.D. Doherty, R. Becker, Acta Mater. **44** (1996) 1233.

3. H.F. Poulsen, L. Margulies, S. Schmidt, G. Winther, Acta Mater. **51** (2003) 3821.

4. R. Becker, S. Panchanadeeswaran, Acta Metall. Mater. **43** (1995) 2701.

5. S.R. Kalidindi, A. Bhattacharyya, R.D. Doherty, Proc. Roy. Soc. London A **460** (2004) 1935.

6. A. Skalli, R. Fortunier, R. Fillit, J.H. Driver, Acta Metall. **33** (1985) 997.

7. R. Fortunier, J.H. Driver, Acta Metall. **35** (1987) 1355.

8. D. Raabe, Z. Zhao, W. Mao, Acta Mater. **50** (2002) 4379.

9. J. Hirsch, K. Lücke, Acta Metall. **36** (1988) 2863.

10. J. Hirsch, K. Lücke, Acta Metall. **36** (1988) 2883.

11. A.J. Beaudoin, P.R. Dawson, KK. Mathur, U.F. Kocks, Inter. J. Plasticity **11** (1995) 501.

12. B. Bay, N. Hansen, D.A. Hughes, D. Kuhlmann-Wilsdorf, Acta Metall. Mater. **40** (1992) 205.

13. Q. Liu, N.Hansen, Phys. Stat. Sol. (a) **149** (1995) 187.

14. Q. Liu, N. Hansen, Mat. Sci. Eng. **A234-236** (1997) 672.

15. X. Huang, N. Hansen, Scripta Mater. **37** (1997) 1.

16. T. Leffers, H. Christoffersen, Mat. Sci. Eng. **A234-236** (1997) 676.

17. X. Huang, Scripta Mater. **38** (1998) 1697.

18. Q.Liu, D. Juul Jesen, N.Hansen, Acta Mater. **46** (1998) 5819.

19. N. Hansen, Metall. Trans. **32A** (2001) 2917.

20. F.J. Humphreys, J. Mat. Sci. **36** (2001) 3833.

21. L. Delannay, O.V. Mishin, D. Juul Jensen, P. Van Houtte, Acta Mater. **49** (2001) 2441.

22. M.Kumar, A.J. Swartz, W.E. King, Mat. Sci. Eng. **A309-310** (2001) 78.

23. D. Chandrasekaran, M. Nygårds, Acta Mater. **51** (2003) 5375.

24. L Delanney, R.E. Logé, Y. Chastel, J.W. Signocelli, P. Van Houtte, Adv. Eng. Materials **5** (2003) 597.

25. J.H. Han, K.-K. Jee, K.H. Oh, Inter. J. Mechanical Sciences **45** (2003) 1613.

26. P. Trivedi, D.P. Field, H. Weiland, Inter. J. Plasticity **20** (2004) 459.

27. D. Raabe, M. Sachtleber, Z. Zhao, F. Roters, S. Zaefferer, Acta Mater. **49** (2001) 3433.

28. M. Sachleber, Z. Zhao, D. Raabe, Mat. Sci. Eng. **A336** (2002) 81.

29. A. Tatschl, O. Kolednik, Mat. Sci. Eng. **A339** (2003) 265.

30. B.M. Schroeter, D.L. McDowell, Inter. J. Plasticity **19** (2003) 1355.

31. D. Raabe, M. Sachtleber, L.F. Vega, H. Weiland, Adv. Eng. Mat. **4** (2004) 859

32. W. Boas, M.E. Hargraves, Proc. Royal Society **A193** (1948) 89.

33. W. Boas, G.J. Ogilvie Acta Metall. **2** (1954) 655.

34. V.M. Urie, H.L. Wain, J Inst. Metals **81** (1952-53) 153.

35. F. Delaire, J.L. Raphanel, C. Rey, Acta Mater. **48** (2000) 1075.

36. C.Y.J. Barlow, B. Bay, N. Hansen, Phil. Mag. A **51** (1985) 253.

37. V. Randle, N. Hansen, D. Juul Jensen, Phil Mag. A **73** (1996) 265.

38. T.J. Sabin, G. Winther, D. Juul Jensen, Acta Mater. **51** (2003) 3999.

39. B.C. Larson, W. Yang, J.Z. Tischler, G.E. Ice, J.D. Budai, W. Liu, H. Weiland, Inter. J. Plasticity **20** (2004) 543.

40. Y.M. Soifer, A. Verdyan, M. Kazakevich, E. Rabkin, Scripta Mater. **47** (2002) 799.

41. S.V. Harren, R.J. Asaro, J. Mech. Physics Solids, **37**, (1989) 191.

42. A.J. Beaudoin, H. Meeking, U.F. Kocks, Phil Mag. A **73** (1996) 1503.

43. D.P. Mika, P.R. Dawson, Acta Mater. **47** (1999) 1355.

44. D. Raabe, Z. Zhao, S.-J. Park, F. Roters, Acta Mater. **50** (2002) 421.

45. U.F. Kocks, H. Chandra, Acta Metall. **30** (1982) 695.

46. T. Leffers, Inter. J. Plasticity **17** (2001) 469.

47. T. Leffers, Inter. J. Plasticity **17** (2001) 491.

48. J.H. Han, S.M. Baeck, K.H. Oh, Y.H. Chung, Mat. Sci. Forum, **408-4** (2002) 203.

49. V.Y. Gertsman, K. Tangri, R.Z. Valiev, Acta Metall. Mater. **42** (1994) 1785.

50. G.I. Taylor, J. Inst. Metals, **61** (1938) 307.

51. J.F.W. Bishop, R. Hill Phil Mag. **42** (1951) 414.

52. R.A. Lebensohn, T. Leffers, Textures and Microstructures **31** (1999) 217.

53. C. Tome, G.R. Canova, U.F. Kocks, N. Christadoulou, J.J. Jonas, Acta Metall. **32** (1984) 1637.

54. G.C. Butler, D.L. Mc Dowell, Inter. J. Plasticity **14** (1998) 703.

55. R.J. Asaro, A. Needleman, Acta Metall. **33** (1985) 923.

56. M. Renouard, M. Wintenberger, C.R. Seanc. Acad. Sci. Paris B, **292** (1981) 385.

57. J.H. Driver, A. Skalli, M. Wintenberger, Phil Mag. A **49** (1984) 505.

58. D.A. Hughes, N. Hansen, Acta Mater. **45** (1997) 3871.

59. D. Raabe, Z. Zhao, F. Roters, Scripta Mater. 50 (2004) 1085.

60. G. Winther, X. Huang, N. Hansen, Act Mater. **48** (2000) 2187.

61. J.A. Wert, X. Huang, Phil Mag. **83** (2003) 969.

Table 1. Crystal orientations in grains α to σ, identified in Fig. 1a.

Grain in Fig. 1a	Crystal direction parallel to TA	Crystal direction parallel to SF
α	[0.694, 0.691, $\overline{0.202}$]	[0.493, $\overline{0.661}$, $\overline{0.565}$]
β	[0.991, 0.096, 0.090]	[$\overline{0.080}$, 0.982, $\overline{0.168}$]
χ	[0.868, 0.472, 0.152]	[0.176, $\overline{0.007}$, $\overline{0.984}$]
δ	[0.851, 0.519, 0.774]	[0.309, $\overline{0.615}$, 0.725]
φ	[0.914, 0.391, $\overline{0.107}$]	[0.111, 0.132, 0.994]
γ	[0.993, 0.120, $\overline{0.002}$]	[0.103, $\overline{0.846}$, 0.522]
η	[0.697, 0.586, 0.413]	[$\overline{0.134}$, $\overline{0.460}$, 0.878]
ι	[0.826, 0.561, $\overline{0.058}$]	[$\overline{0.483}$, 0.651, $\overline{0.586}$]
φ	[0.742, 0.638, $\overline{0.205}$]	[$\overline{0.654}$, 0.624, $\overline{0.247}$]
κ	[0.847, 0.532, 0.006]	[0.057, $\overline{0.079}$, $\overline{0.995}$]
λ	[0.992, 0.124, 0.025]	[$\overline{0.050}$, 0.568, $\overline{0.821}$]
μ	[0.754, 0.600, $\overline{0.265}$]	[0.073, 0.325, 0.943]
ν	[0.814, 0.476, 0.331]	[0.579, $\overline{0.688}$, $\overline{0.436}$]
o	[0.790, 0.594, 0.151]	[0.586, $\overline{0.58}$, $\overline{0.474}$]
π	[0.870, 0.433, $\overline{0.234}$]	[0.108, 0.296, 0.949]
θ	[0.797, 0.482, $\overline{0.364}$]	[0.389, $\overline{0.870}$, $\overline{0.302}$]
ρ	[0.825, 0.467, 0.331]	[$\overline{0.248}$, $\overline{0.234}$, 0.940]
σ	[0.827, 0.558, $\overline{0.065}$]	[0.488, $\overline{0.656}$, 0.576]
τ	[0.834, 0.551, 0.028]	[0.413, $\overline{0.591}$, $\overline{0.692}$]

Table 2. Shear amplitude factors corresponding to the Taylor solutions (designated T1-T12) for three different imposed strain states. Slip systems are designated using the standard notation [51] with slip plane n and Burgers vector b. The Schmid factor for uniaxial tension is designated m.

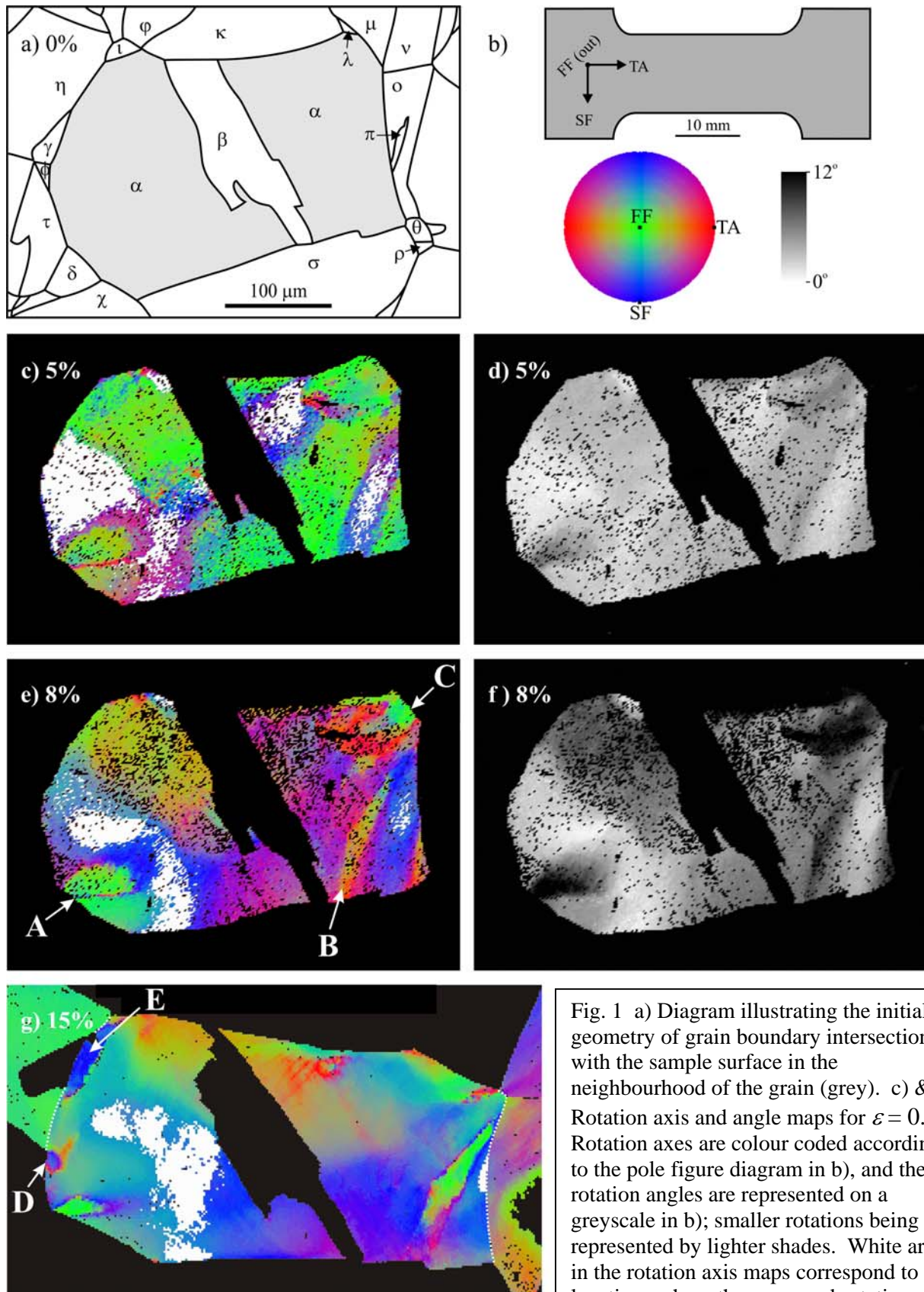| Strain state	M		a1	a2	a3	b1	b2	b3	c1	c2	c3	d1	d2	d3
		$n\rightarrow$	(111)	(111)	(111)	$(\bar{1}\bar{1}1)$	$(\bar{1}\bar{1}1)$	$(\bar{1}\bar{1}1)$	$(\bar{1}11)$	$(\bar{1}11)$	$(\bar{1}11)$	$(1\bar{1}1)$	$(1\bar{1}1)$	$(1\bar{1}1)$
$\downarrow$	$\downarrow$	$b\rightarrow$	$[01\bar{1}]$	$[\bar{1}01]$	$[1\bar{1}0]$	$[0\bar{1}\bar{1}]$	$[101]$	$[\bar{1}10]$	$[01\bar{1}]$	$[101]$	$[\bar{1}\bar{1}0]$	$[0\bar{1}\bar{1}]$	$[\bar{1}01]$	$[110]$
$\begin{pmatrix} \varepsilon & 0 & 0 \\ 0 & -\varepsilon/2 & 0 \\ 0 & 0 & -\varepsilon/2 \end{pmatrix}$	3.5	T1$\rightarrow$	43	-21	0	0	0	0	-7	0	0	-21	7	0
		T2$\rightarrow$	21	-43	0	0	0	0	-7	21	0	0	7	0
		T3$\rightarrow$	21	-21	0	0	-21	0	-7	0	0	0	29	0
		T4$\rightarrow$	21	-21	0	0	21	0	-29	0	0	0	7	0
		$m\rightarrow$	0.43	-0.43	0.00	0.32	-0.32	0.00	-0.07	-0.04	0.11	0.04	0.07	-0.11
$\begin{pmatrix} \varepsilon & \varepsilon/2 & 0 \\ \varepsilon/2 & -\varepsilon/2 & 0 \\ 0 & 0 & -\varepsilon/2 \end{pmatrix}$	3.9	T5$\rightarrow$	0	-12	0	1	-55	0	0	0	0	0	31	0
		T6$\rightarrow$	0	-43	0	1	-24	0	0	31	0	0	0	0
		T7$\rightarrow$	0	-12	0	32	-24	0	-31	0	0	0	0	0
		T8$\rightarrow$	31	-12	0	1	-24	0	0	0	0	-31	0	0
$\begin{pmatrix} \varepsilon & 0 & -\varepsilon/2 \\ 0 & -\varepsilon/2 & 0 \\ -\varepsilon/2 & 0 & -\varepsilon/2 \end{pmatrix}$	3.8	T9$\rightarrow$	43	-1	0	24	0	0	0	0	0	-23	9	0
		T10$\rightarrow$	19	-25	0	24	0	0	0	23	0	0	9	0
		T11$\rightarrow$	19	-1	0	47	0	0	-23	0	0	0	9	0
		T12$\rightarrow$	19	-1	0	24	-23	0	0	0	0	0	32	0

Fig. 1 a) Diagram illustrating the initial geometry of grain boundary intersections with the sample surface in the neighbourhood of the grain (grey). c) & d) Rotation axis and angle maps for $\varepsilon = 0.05$. Rotation axes are colour coded according to the pole figure diagram in b), and the rotation angles are represented on a greyscale in b); smaller rotations being represented by lighter shades. White areas in the rotation axis maps correspond to locations where the measured rotation angle was less than 2°. e) & f) Rotation axis and angle maps for $\varepsilon = 0.08$. g) Rotation axis map for $\varepsilon = 0.15$.
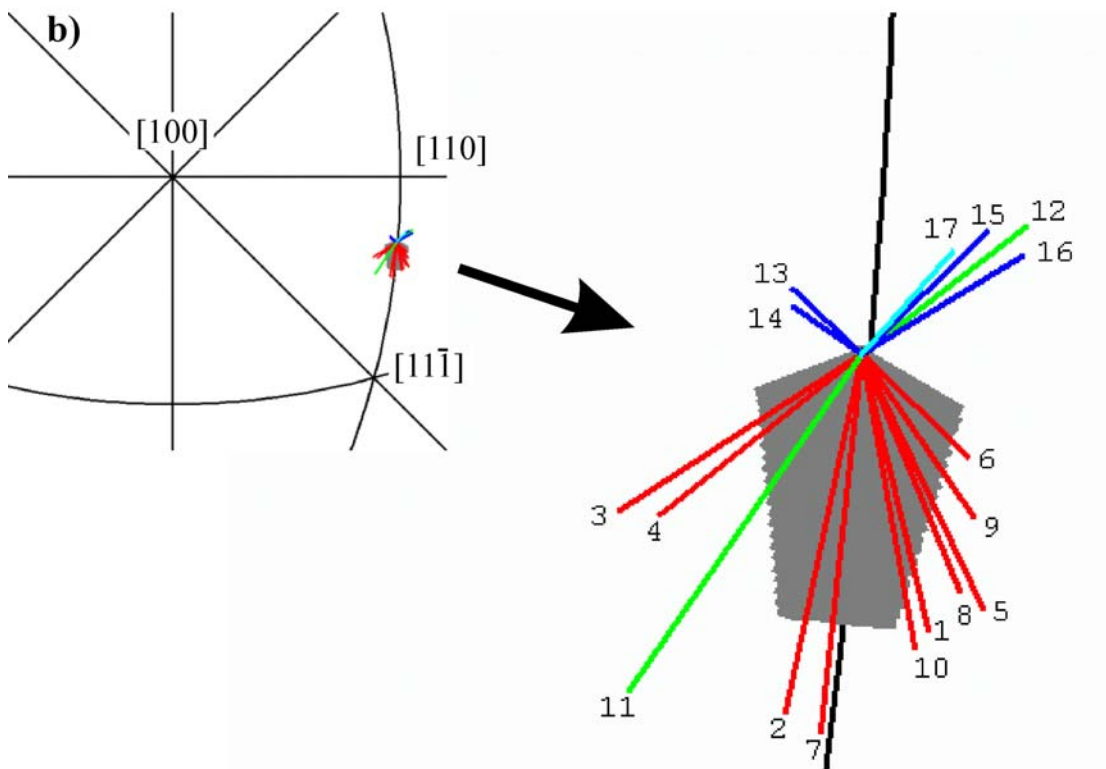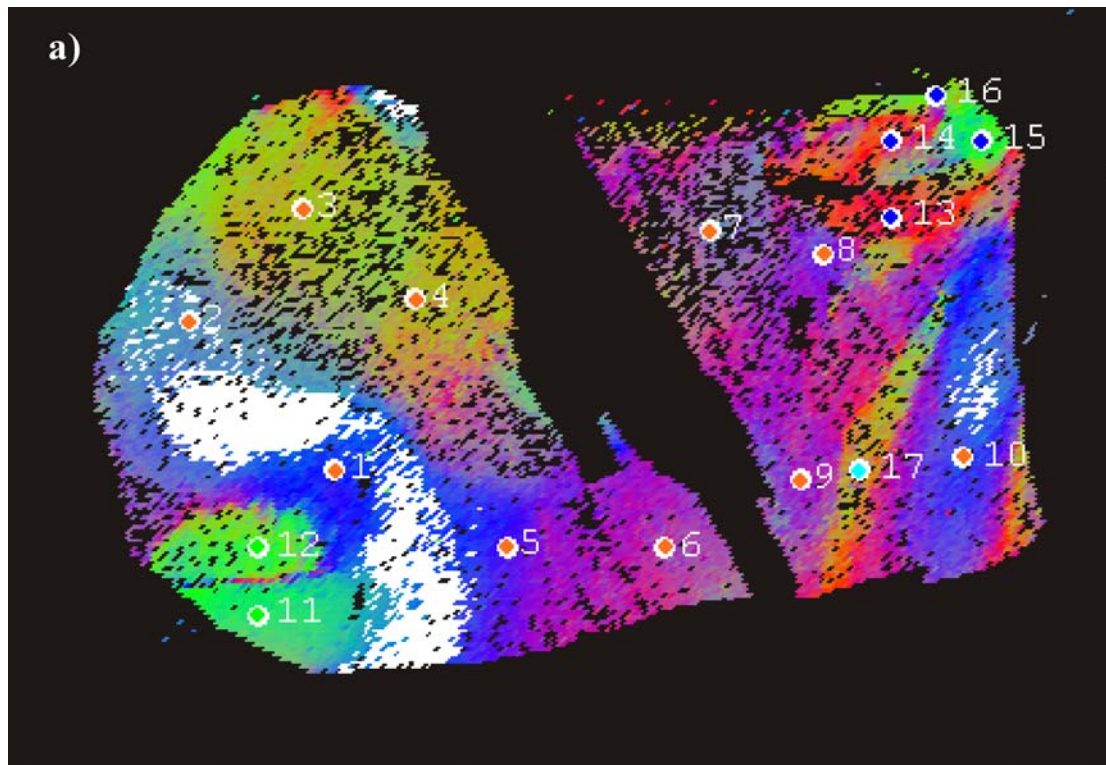
Fig. 2 a) Rotation axis map for $\varepsilon = 0.08$ with the locations of points 1 – 17 identified. Points 1 – 10 (red) represent coarse orientation domains. Points 11 – 12 (green), 13 – 16 (dark blue), 17 (light blue) are representative of features A – C. b) Stereographic projection showing change in tensile axis orientation for the individual points as well as the range of tensile axis rotations predicted by the Taylor solutions for this grain (grey polygon).
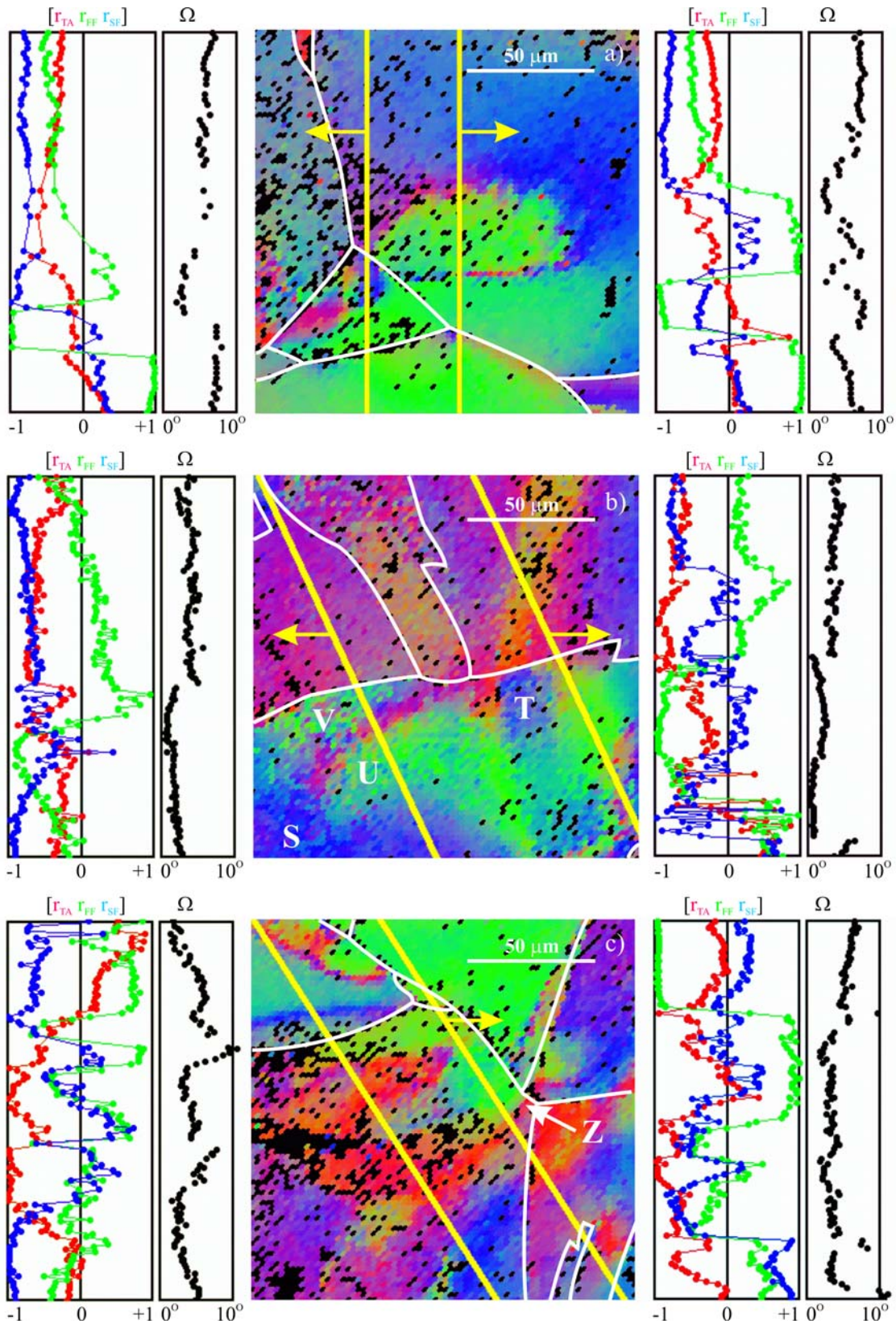
Fig. 3 Detailed rotation axis maps for the central grain and adjacent grains in the vicinity of Features A – C. The plots to the left and right of each rotation axis map show the variation of **R** components and Ω as a function of distance along the yellow reference lines.
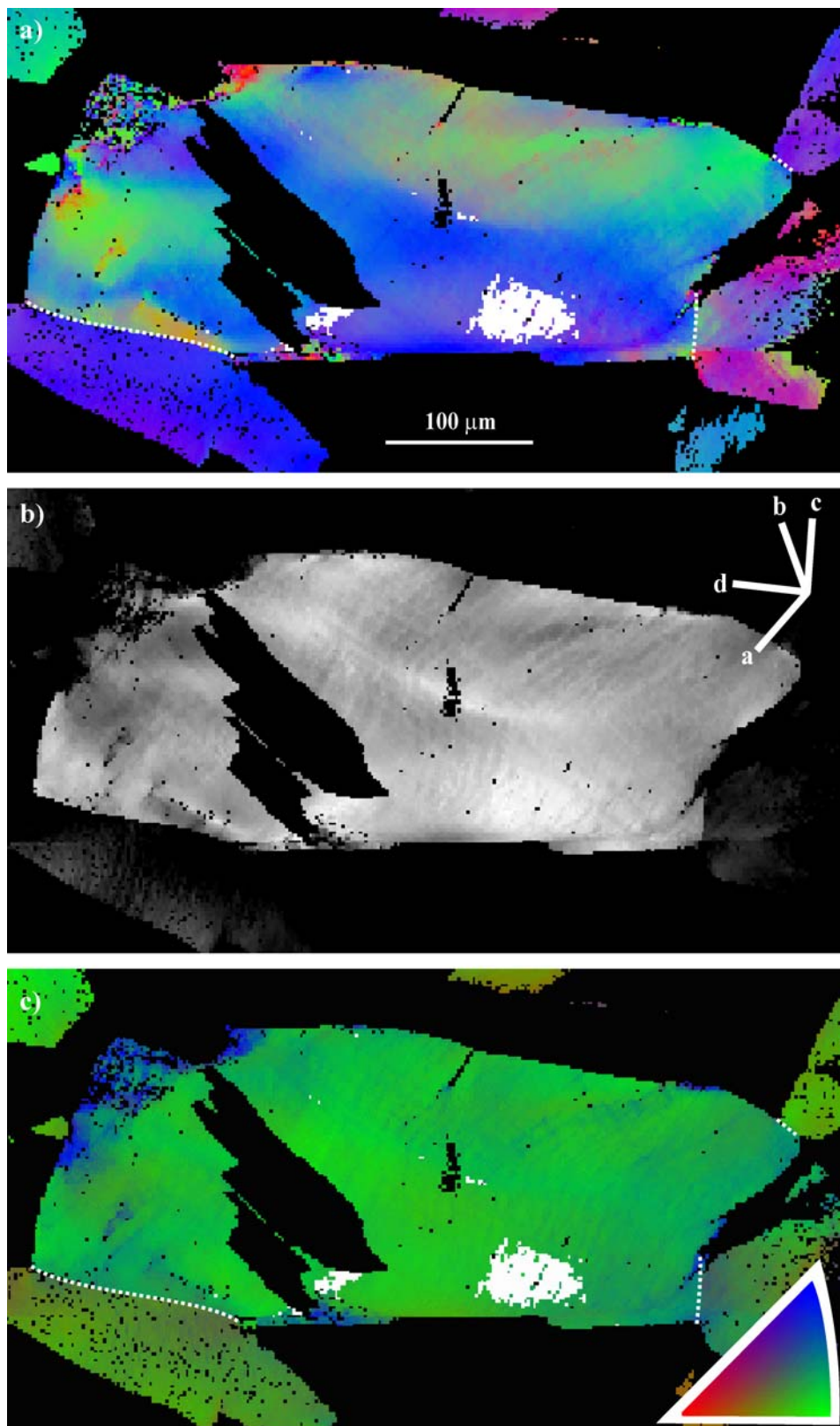
Fig. 4 a) Rotation axis map and b) rotation angle map for the grain at $\varepsilon = 0.25$. The slip traces for slip planes $a - d$ correspond to slip plane orientations in the initial crystal. orientation. c) Alternate colour coding method mapping components uvw (crystal direction parallel to TA) to RGB.
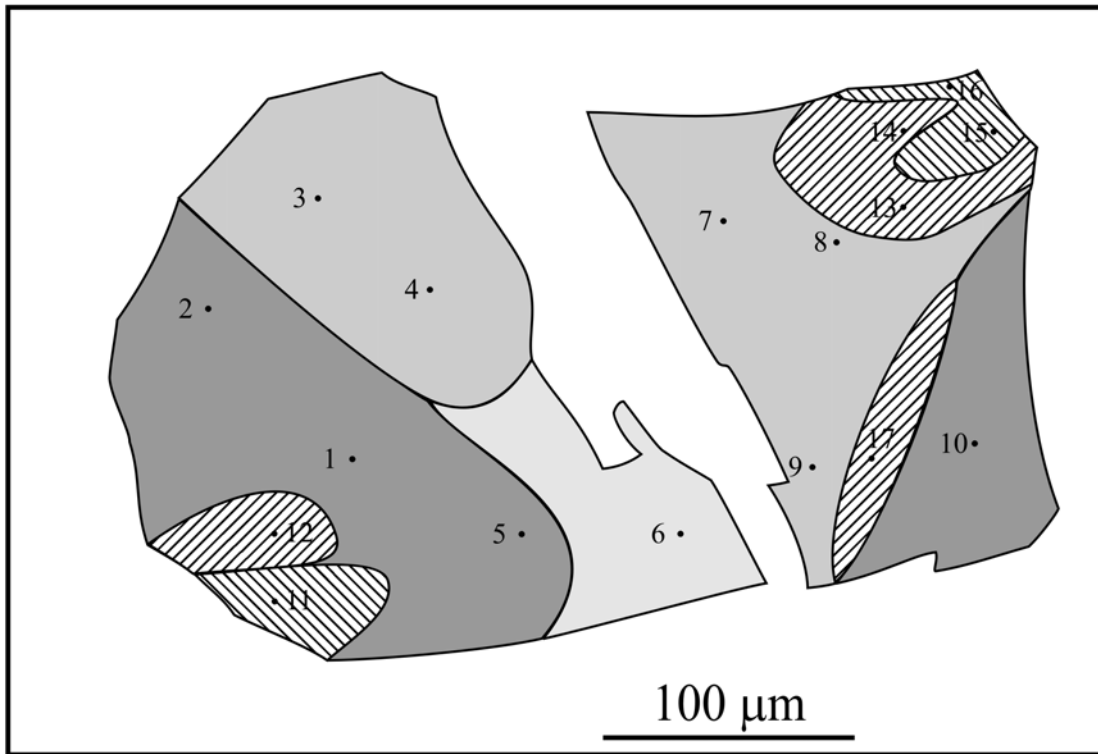
Fig. 5 Schematic diagram showing the domain structure of the grain at $\varepsilon = 0.08$. The grey shaded regions are coarse domains and the hashed regions are grain interaction domains.
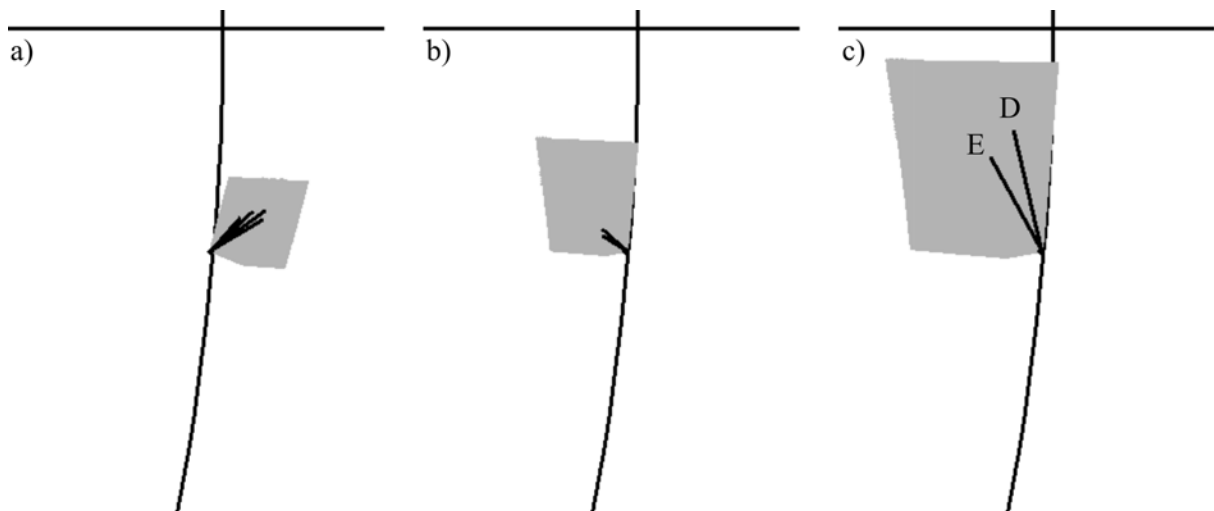

Fig. 6 Stereographic projection representations of measured tensile axis rotations for a) Points 12, 15 - 17. b) Points 13 and 14. c) Features D and E. The measurements are superposed on the full range of Taylor solutions for a) & b) $\varepsilon = 0.08$, c) $\varepsilon = 0.15$.